Applied Surface Science 631 (2023) 157582

Contents lists available at ScienceDirect

Applied Surface Science

journal homepage: www.elsevier.com/locate/apsusc

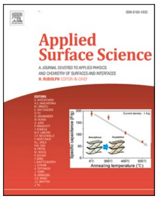

Full Length Article

Fine-tuning of plasmonics by Au@AuY/Au core–shell nanoparticle monolayer for enhancement of third-order nonlinearity

Yong Liu [a], Chi Pang [b], Hiroshi Amekura [c], Thomas Schumann [d], Peng Liu [a], Zhixian Wei [a], Haocheng Liu [e], Rang Li [d,*]

[a] Institute of Frontier and Interdisciplinary Science and Key Laboratory of Particle Physics and Particle Irradiation (MOE), Shandong University, Qingdao, Shandong 266237, China
[b] Institute for Emerging Electronic Technologies, Leibniz IFW Dresden, Dresden 01069, Germany
[c] National Institute for Materials Science (NIMS), Tsukuba 305-0003, Japan
[d] Institute of Ion Beam Physics and Materials Research, Helmholtz-Zentrum Dresden-Rossendorf, Dresden 01328, Germany
[e] State Power Investment Corporation Research Institute, Beijing 102209, China

ARTICLE INFO

Keywords:
Plasmonics
Core-shell alloy nanostructure
Localized surface plasmon resonance
Third-order nonlinearity
Sequential ion implantation

ABSTRACT

The manipulation of plasmonics on noble metal nanoparticles (NPs) is of great interest in developing nonlinear photonic devices, such as all-optical switches and frequency combs. An Au@AuY-core/Au-shell nanoparticle (Au@AuY/Au NP) monolayer is proposed for the fine-tuning of plasmonics and enhanced third-order nonlinearity. Based on the different thermodynamic mechanisms of Au and Y ions, the compact Au@AuY/Au core–shell architectures are designed and surface-modified in fused silica (SiO_2) with enhanced free electron density, mobility, and quantum size effect. The flexible modulation of plasmonics is realized, resulting in significant absorption enhancement (165% for interband absorption and 38% for free electron absorption, respectively) and fine-tuning of the localized surface plasma resonance (LSPR) band. In addition, the physical mechanism is investigated by density functional theory (DFT) and Mie theory, which reveals a transition from size-independence to size-dependence of LSPR owing to the synergistic effect of multiple physical factors such as free electron density and mobility. With the above advantages, the third-order nonlinearity is enhanced by 4.4 times compared with traditional Au NPs. It indicates the significant potential of Au@AuY/Au core–shell NP monolayer in the performance improvement of nonlinear photonic devices.

1. Introduction

Plasmonics manipulation has become one of the most attractive topics due to its critical role in various photonic applications, such as plasmonic tweezers, solar cells, ultrafast lasing and super-resolution imaging [1–8], etc. Based on the surface modified technologies, the plasmonics on nanomaterials (e.g., metal and semiconductor nanostructures) can be flexibly manipulated [9–12], resulting in tunable localized surface plasmon resonance (LSPR) phenomenon in frequency and spatial domains. To date, previous studies have indicated the possibility of the controllable plasmonic band and near-field distribution on doped semiconductor metasurface by tunable free electron density and mobility [13,14]. However, the fine-tuning of plasmonics on metal nanostructures is difficult to realize because of the fixed physical parameters of electrons in metals. Instead, the contribution of metallic morphology to the LSPR modulation is generally considered [15–17], which provides efficient tuning of spatial distribution by reconstruction of metal nanostructures. Although there is considerable progress in this field, the technical difficulty of morphology modification with high precision hinders its development in practical applications. Since the performance (e.g., third-order nonlinearity) of metal-based plasmonic devices strongly depends on the frequency and spatial distribution of LSPR [18,19], it is of significant importance to realize precise manipulation of plasmonics by combining the modified electron parameters and morphology of nanostructures.

Since it was reported in the early 1990 s [20,21], core–shell NPs have been attracting a lot of interest owing to their conducive and versatile compositions and structures to serve multi-functional capabilities and enhanced properties. The shell material coating can provide tunable surface functions, improve the stability and reduce the consumption of

---

* Corresponding author.
E-mail address: r.li@hzdr.de (R. Li).

https://doi.org/10.1016/j.apsusc.2023.157582
Received 9 March 2023; Received in revised form 16 May 2023; Accepted 20 May 2023

precious materials [22], which enables core–shell NPs as an emerging nanomaterial for various applications, such as dye sensitized solar cells, biomedical and catalysis [22,23]. For plasmonic core–shell NPs, the LSPR-induced linear and nonlinear optical properties can be optimized by designing the composition and the ratio of core and shell [24,25]. Thus, based on the plasmonic metal NP platform, a novel core–shell configuration can be designed with tunable free electron density and mobility by serving the modified surface of the core as the shell of NPs. Recent developments in the field of ion beam technology have provided the possibility for the fabrication of such unique core–shell NPs [26]. In general, energetic heterogeneous metal ions are implanted into the dielectric materials and aggregate to spherical hybrid metal NPs spontaneously when the concentration exceeds solid solubility. During thermal annealing, diverse metal ions will diffuse into the core and shell of the NPs due to the different diffusion efficiency constants. Compared with the other plasmonics manipulation methods in solid dielectrics [27,28] (e.g., optical traction and femtosecond laser induction), ion beam technology [29–31] shows the advantages of unlimited species of dielectrics, quantitatively controlled precise construction of NPs, gradient surface modification and suitability for industrial mass production.

In this work, Au@AuY/Au NPs are proposed by sequential ion implantation. In variance to the traditional core–shell NPs fabricated by ion beam, the thermodynamics mechanism of Au and Y ions are additionally considered in this work for a hybrid shell with a controllable element ratio. The morphology characterization and corresponding physical mechanism are investigated experimentally and theoretically. Furthermore, the fine-tuning of plasmonics in frequency and spatial domains are realized with enhanced LSPR response and third-order nonlinearity, which indicates significant potential in optimizing the performance of plasmonics-based photonic devices.

2. Methods

Sample preparation: The optically polished SiO_2 wafers with dimensions of $10 \times 10 \times 1$ mm^3 were used in this work. As shown in Fig. 1, the two-step ion-implantation experiments followed by thermal annealing were carried out for the core/shell NP fabrication: (i) Firstly, pristine SiO_2 samples were directly implanted with 70 keV Au ions at 300 K to a fluence of 3×10^{16} cm^{-2} to form small Au NPs (sample Au:SiO_2); (ii) Secondly, the Au:SiO_2 samples were subsequently implanted with 150 keV Y ions at 300 K to a fluence of 5×10^{16} cm^{-2} (sample YAuSiO_2); (iii) Finally, the Au:SiO_2 and Y:Au:SiO_2 samples were isochronally annealed in a reducing atmosphere (5 %–H_2 + N_2) at 1100 °C for 60 min (sample annealed Au:SiO_2 and sample annealed Y:Au:SiO_2). During the annealing process, the implanted Au atoms may aggregate and form Au NP, while the isolated Y ions may migrate towards the sample surface, bond with Au atoms and form AuY alloy at the Au NP surface, i.e., AuY/Au nanocomposite shell. Therefore, the Au@AuY/Au NPs are fabricated with an Au core and AuY/Au nanocomposite shell. The reason for the formation of the core–shell structure is that the thermal treatment triggers the diffusion-driven [32] Au NPs growth, the Y atom to the surface of the sample, and the combination of Au and Y. In addition, Y ions are individually implanted into the SiO_2 substrate and annealed at the same conditions as the reference samples (sample Y:SiO_2 and sample annealed Y:SiO_2).

Microstructural characterization: Transmission electron microscopy (TEM) was applied for microstructural analyses. Focused ion beam milling with lift-out processing on an FEI Helios NanoLab 600 Dual Beam system was utilized to prepare cross-sectional TEM samples. An FEI Tecnai G2 F20 transmission electron microscope was used for the TEM, high-resolution TEM (HRTEM), and energy dispersive X-ray spectrometry (EDS) mapping. Notably, the TEM observation time for each sample was kept relatively short so that the electron beam

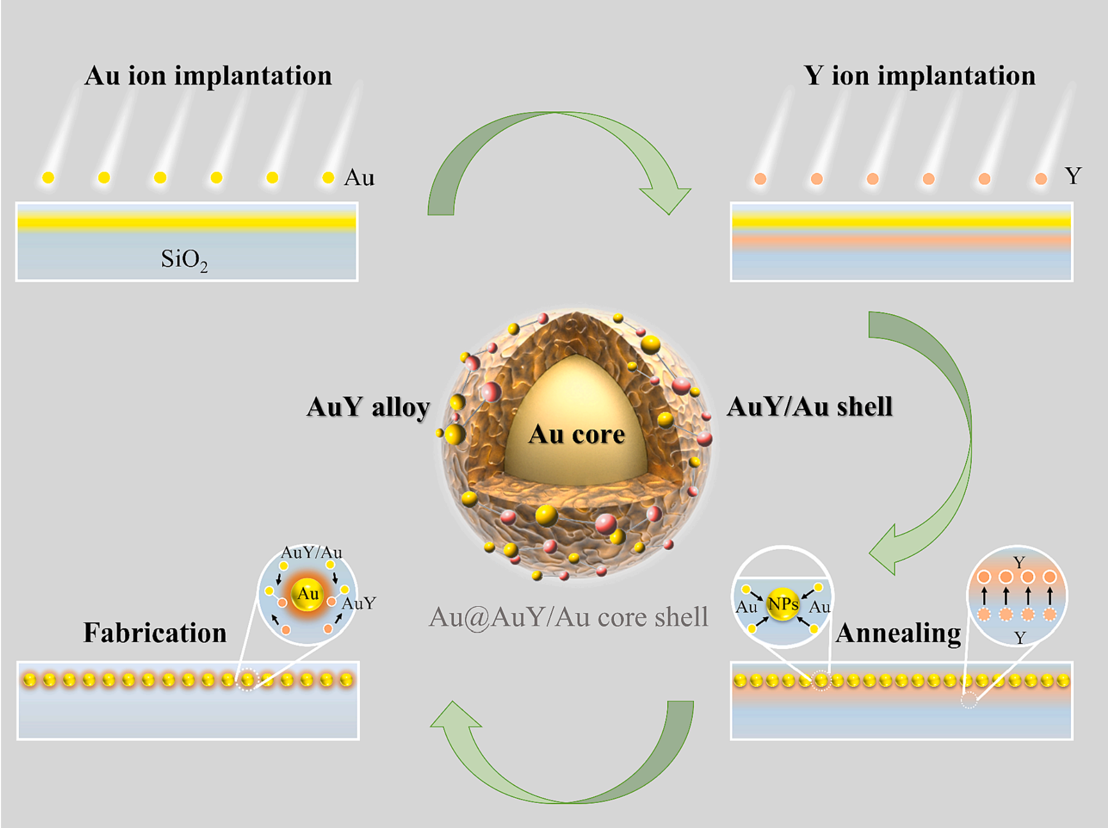

Fig. 1. The schematic diagram of the sample preparation process. Yellow and red particles on the NP surface represent Au and Y atoms, respectively. (For interpretation of the references to colour in this figure legend, the reader is referred to the web version of this article.)

irradiation did not generate noticeable annealing and the recrystallization of damaged lattices [33].

Linear and nonlinear optical measurement: The UV–vis-NIR spectrophotometry (Solid Spec 3700DUV, Shimadzu) was utilized to measure the linear optical absorption spectrum of NPs in SiO_2 within the wavelength range from 200 to 700 nm. The nonlinear optical properties of the samples were characterized by a typical open aperture Z-scan system with an excitation of 532 nm. The pulse width, repetition rate and energy are 4 ns, 20 Hz and 12 μJ, respectively.

Simulations: The depth profiles of Au and Y concentration were determined through the Stopping and Range of Ions in Matter (SRIM) 2013 full-cascade simulation code [34], which is shown in Supplementary Material Fig. S1. For binding energy calculations of Au_n and Au_nY, the geometry of all molecules was optimized through DFT, which is shown in Supplementary Fig. S2. And all the DFT computations were performed at the B3LYP/SDD theoretical level with the GD3BJ dispersion correction [35,36]. All these calculations were performed with Gaussian 16 software package. The LSPR absorption spectrum is simulated based on the Mie theory combined with electron mean free path theory. The near-field distribution of core–shell NP and Au NP is simulated by DDSCAT software [37]. A simplified model of core–shell NP is used in the simulation with a shell of Au/AuY nanocomposite and a core of pure Au.

3. Results and discussion

3.1. Microstructure description and relevant features of Au@AuY/Au core–shell NPs

observations were performed on sample cross-sections to visually characterize and confirm the structural evolution during the fabrication process. As shown in Fig. 2(a), Au-implantation leads to the formation of a crystalline small Au NPs region with a thickness of approximately 67 nm below the sample surface, which can be confirmed by the corresponding EDS mapping, HRTEM image and corresponding FFT image (Fig. 2(b-d)). It indicates the nucleation of Au and the formation of NPs due to the higher concentration of Au ions than the solubility of substrate. Nucleation occurs to aggregate monomers to dimers, trimers, etc. when the concentration of Au atoms approaches the solubility threshold. Ultimately, spherical NPs are formed as a result of the continuous growth of these polymers caused by monomer diffusion and interfacial reaction absorption [18]. After post-implantation thermal annealing, the aggregation of small Au NPs can be accelerated to form large Au NPs even Au islands because of the Ostwald ripening effect [38]. As displayed in Fig. 2(e) and (f), sandwich-like hierarchical nanostructures are observed in sample annealed Au:SiO_2. From top to bottom, a crystalline Au NPs layer, a Au island layer and an amorphous Au NP layer are stacked in order, which is characterized by the HRTEM image and the corresponding FFT image (Fig. 2(g-j), Fig. 2(l) and (m)). In addition, as shown in Fig. 2(k) and (n), the average sizes of crystalline and amorphous Au NPs are 11.3 nm and 23.5 nm, respectively. Furthermore, microstructures of sample Y:SiO_2, sample annealed Y:SiO_2 and sample Y:Au:SiO_2 are shown in Supplementary Material Fig. S3-S5.

For the sample annealed Y:Au:SiO_2, a uniformed NP monolayer with some dispersed small NPs deeper is found as seen in Fig. 2(o). The spatial distribution of Au and Y elements is displayed in Fig. 2(p) and (q), which exhibits the multi-component composition of NPs. Furthermore, HRTEM image (Fig. 2(r)) of a typical NP confirm that these NPs remain crystalline state, and the corresponding FFT image (Fig. 2(s)) show two sets of diffraction spots representing Au and AuY. Compared with the unannealed Y:Au:SiO_2 sample (see Supplementary Material Fig. S5), the Y atoms of annealed Y:Au:SiO_2 tend to move toward the free surface, which is attributed to the action of the stress gradient induced by ions implantation and the temperature field [39]. In addition, the average diameters of the dispersed small NPs and large NPs are approximately 5.2 and 21.4 nm, respectively, as shown in Fig. 2(t).

To further understand the detailed nanostructure and the formation dynamics of the NPs in annealed Y:Au:SiO_2 sample, EDS line-scan analysis was carried out, and the results are shown in Fig. 3(a). Considering the spherical shape of NPs, the relative content distributions of Au and Y elements along the radius were obtained based on the mathematical calculation of the line scanning results (see empirical formulas (2) and (3) in Supplementary Material). As shown in Fig. 3(b), the relative content of Au is smaller in the central region of the nanoparticles, which is attributed to the diffusion effect of Au ions and the aggregation of defects (nanovoids) during the annealing process [40]. Noted that Y atoms are mainly distributed away from the NP center, i.e., located at the near surface of NPs. Therefore, the nanostructure of NP can be regarded as a core–shell NP composed of Au core and Au/AuY nanocomposite shell. Furthermore, the HAADF signal intensity obtained from line profiles across the NP shows a contrast change similar to the elemental relative content calculations, as can be observed in Fig. 3(c). Obviously, the lower (high) intensity at NP core (shell) means the smaller (larger) average relative atomic mass, which origins from the nanovoids (Y ions) and Au ions at NP core (shell). The intensity difference between experimental and calculation is caused by the ignorance of X-ray reabsorption in calculation and inhomogeneity of element distribution in experiment, which results from the different thermodynamic process of Au and Y. In order to investigate the combination form of Au and Y atoms, the binding energies of some Au_n and Au_nY, which are widely used to determine the stability of a defect cluster complex [41], were calculated using DFT, and the results are shown in Fig. 3(d). In this work, for Au_n ($n = 3$–10) binding energy per atom (E_b/n) values, defined as $[E(Au_n)\text{-}nE(Au)]/(n\text{-}1)$; For Au_nY ($n = 3$–10) binding energy per atom (E_b/n) values, defined as $[E(Au_nY) - nE(Au) - E(Y)]/n$. The negative value of binding energy indicates the reasonability of the formation of stable Au_n and Au_nY structure, and the higher absolute value means the more stable nanostructure. As seen, the absolute value of the binding energy of Au_n varies slightly when more Au atoms are added, whilst that of Au_nY decreased obviously with the increase of n. It indicates that the existing form of AuY has the maximum stability compared with the form with high content of Au. Therefore, the dynamics process can be described as follows. In the beginning, the implanted Y ions are distributed much deeper compared with the Au ions (Supplementary Material S1). During the annealing, small Au NPs aggregate to large NPs and grow larger. Meanwhile, Y ions migrate to the sample surface and are combined with Au atoms on the NP surface. Since the stability of AuY is greater than the other form (such as Au_2, Au_3, Au_2Y, Au_3Y….), Au atoms prefer to combine with Y ions rather than the other Au atoms avoiding the overgrowth of Au NPs due to the Ostwald ripening effect. As a result, the AuY and Au nanocomposite is formed as the shell of NP with pure Au core, which is verified by the FFT results.

3.2. Tailoring of optical properties of dielectrics by Au@AuY/Au core–shell NPs

The linear and nonlinear optical responses of the plasmonic NPs are investigated and the linear absorption spectrum of the sample annealed Au:SiO_2 and sample annealed Y:Au:SiO_2 are depicted in Fig. 4(a). As seen, the typical LSPR absorption peak is located at 550 nm (538 nm) for the sample annealed Au:SiO_2 (Y:Au:SiO_2), in the meanwhile, a dramatic increase of absorption is observed at the ultraviolet band. It is known that the absorption peak at the visible band is contributed to the free carrier absorption, and the interband absorption at the ultraviolet band comes from the transition of electrons from the occupied d-level state to an empty state in the conduction band above the Fermi level [42]. For a better comparison, the absorption spectrum is mathematically divided into several peaks according to free carrier absorption and interband absorption. Noted that an additional free carrier absorption peak is obtained for the sample annealed AuSiO$_2$, which is possible due to the existence of different kinds of Au NPs (crystalline and amorphous). As shown in Fig. 4(b), the interband absorption spectrum is displayed by

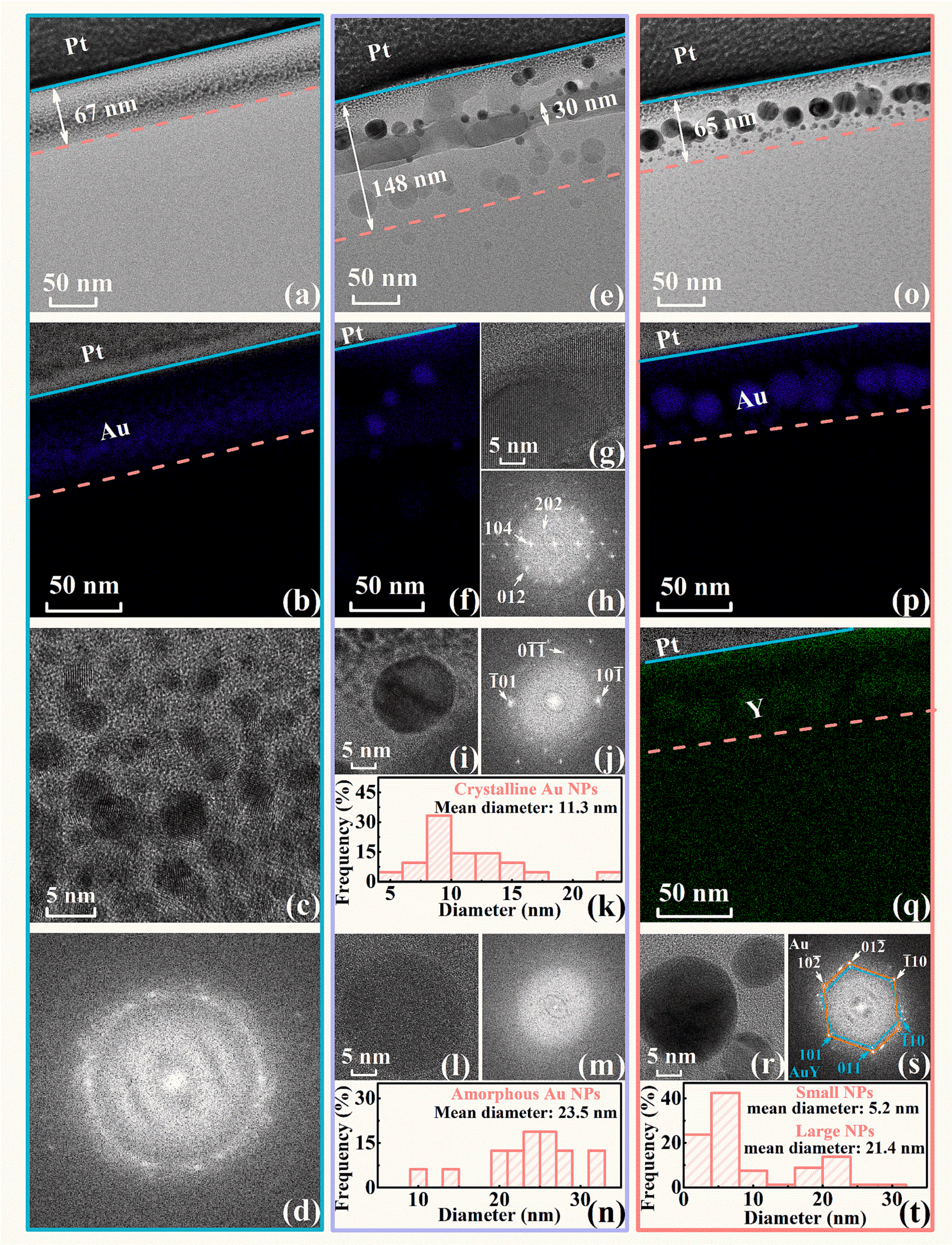

Fig. 2. Sample Au:SiO_2: (a) TEM image, (b) EDS mapping, (c) HRTEM image and (d) corresponding FFT image of the small Au NPs region; Sample annealed Au:SiO_2: (e) TEM image, (f) EDS mapping, (g) HRTEM image and (h) corresponding FFT image of the Au islands, (i) HRTEM image and (j) corresponding FFT image of the crystalline Au NPs, (k) diameter distribution of the crystalline Au NPs, (l) HRTEM image and (m) corresponding FFT image of the amorphous Au NPs, (n) diameter distribution of the amorphous Au NPs; Sample annealed Y:Au:SiO_2: (o) TEM image, (p) and (q) EDS mapping, (r) HRTEM image and (s) corresponding FFT image of a typical NP, (t) diameter distribution of the NPs.

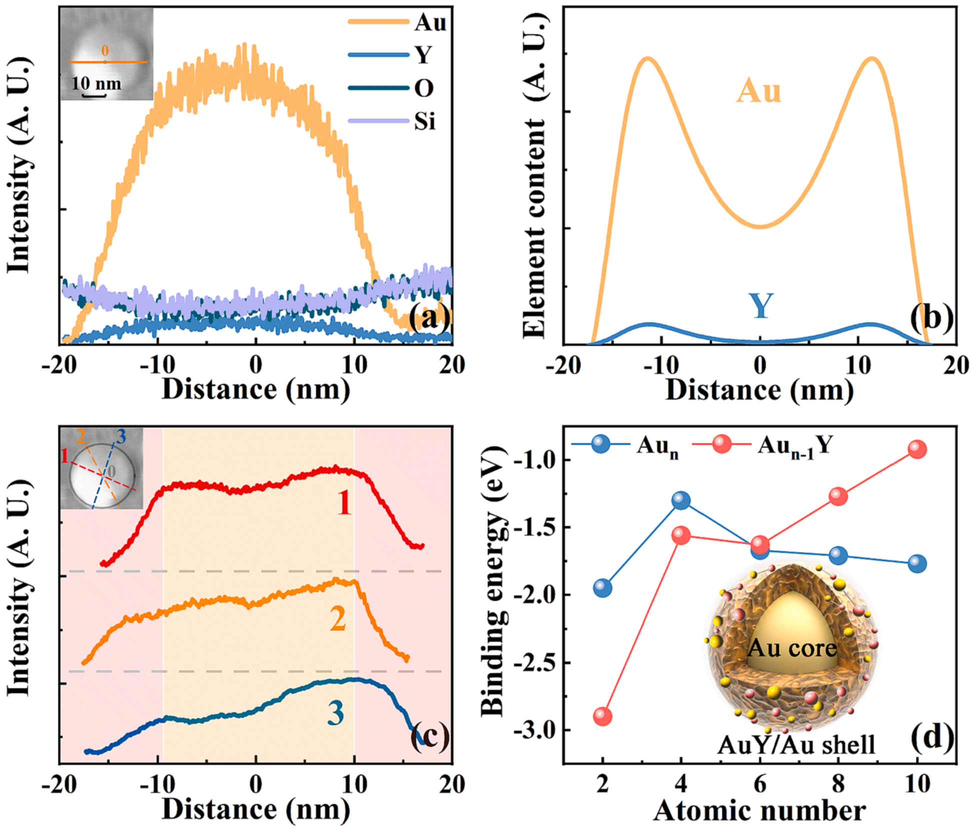

Fig. 3. (a) Line-scan EDS spectrum of a typical NP in sample annealed Y:Au:SiO_2. (b) The relative content distributions of Au and Y elements along the radius. (c) The HAADF signal intensity obtained from line profiles across the NP. (d) The binding energies of some Au_x and Au_xY were calculated using DFT.

normalizing the LSPR peaks of both samples. Obviously, the interband absorption of sample annealed $YAuSiO_2$ is significantly increased by more than 165 % with a steep absorption edge. The enhanced intensity is caused by the formation of perfect spherical NPs without Au island, which weakens the quantum size effect induced energy level splitting phenomenon [42]. Moreover, the scattering effect of the small Au NPs below may also contribute to the enhancement [19]. The narrowed peak means the Au@AuY/Au NPs with uniform size on the same interband transition energy, while the interband transition energy of NPs in sample annealed Au:SiO_2 varies with the size distribution resulting in the wide interband absorption. It should be noted that the weak and ultra-broad absorption peak at the visible band may be caused by the absorption of small Au NPs, which is not considered in the mathematical peak dividing. As for the free carrier absorption, as shown in Fig. 4(c), there are two sets of absorption systems with different peak positions in sample annealed Au:SiO_2, which are ascribed to crystalline and amorphous Au NPs, respectively. Compared with the sample annealed Au:SiO_2, the absorption peak of the sample annealed Y:Au:SiO_2 shows an obvious blue shift with enhanced intensity by 38 % at 532 nm.

The physical mechanism is investigated by Mie theory simulation combined with electron mean free path theory modified Drude model [43]:

$$A=\frac{18\pi\rho\varepsilon_{SiO_2}^{3/2}}{\lambda}\frac{\varepsilon_{Au}^{''}}{|\varepsilon_{Au}+2\varepsilon_{SiO_2}|} \tag{1}$$

$$\gamma(d)=\gamma+\frac{2V_F}{d} \tag{2}$$

$$\gamma=\frac{e}{\mu m}=\frac{Ne^2\rho}{m} \tag{3}$$

$$V_F=\frac{h}{2\pi m}(3\pi^2N)^{1/3} \tag{4}$$

where A is the absorption coefficient and volume fraction p of Au is estimated as 0.1. The imaginary part of the complex dielectric constant of Au (ε_{Au}) and substrate (ε_{SiO_2}) are marked with superscript $''$. The $\gamma, V_F, e, \rho, m, Nandh$ represent the damping factor, Fermi velocity, electron charge, resistance rate, electron mass, free electron density and Planck constant, which will be used for dielectric constant calculation in the Drude model. In addition, the free electron density and mobility are considered as a variable for dielectric constant modification. More details of the simulation are provided in the Supplementary Material. As displayed in Fig. 4(d), the simulated and experimental results meet a good agreement that the absorption peaks of crystalline and amorphous Au NPs are located at 551 nm and 561 nm, respectively. The reason for the difference is believed to be the modified electron mean free path. The electron mean free path of amorphous NP will be reduced resulting in the red-shift of the plasmonic peak, which has been proved based on amorphous Cu NPs [44]. According to the simulation results, the relaxation time of amorphous Au NP is determined to be 0.22 times smaller compared to that of crystalline Au NP, which is similar to the value in the literature [44]. Different from the above peak shift direction, Au@AuY/Au core–shell NPs show an obvious blue shift from 551 nm to 538 nm. It is well known that the peak shift is mainly related to factors including NP size and reflective index of the dielectric environment [45]. However, the former one doesn't show an obvious effect according to the simulated size dependent absorption spectrum (Fig. 4(e)), while the latter one can only lead to the red-shift of peak because of the enhanced reflective index of SiO_2 after ion implantation. Therefore, the fine-tuning of plasmonics is believed to be caused by the surface modification of the AuY/Au shell. As shown in Fig. 4(f), the LSPR absorption is investigated by considering the shell-core structure as a

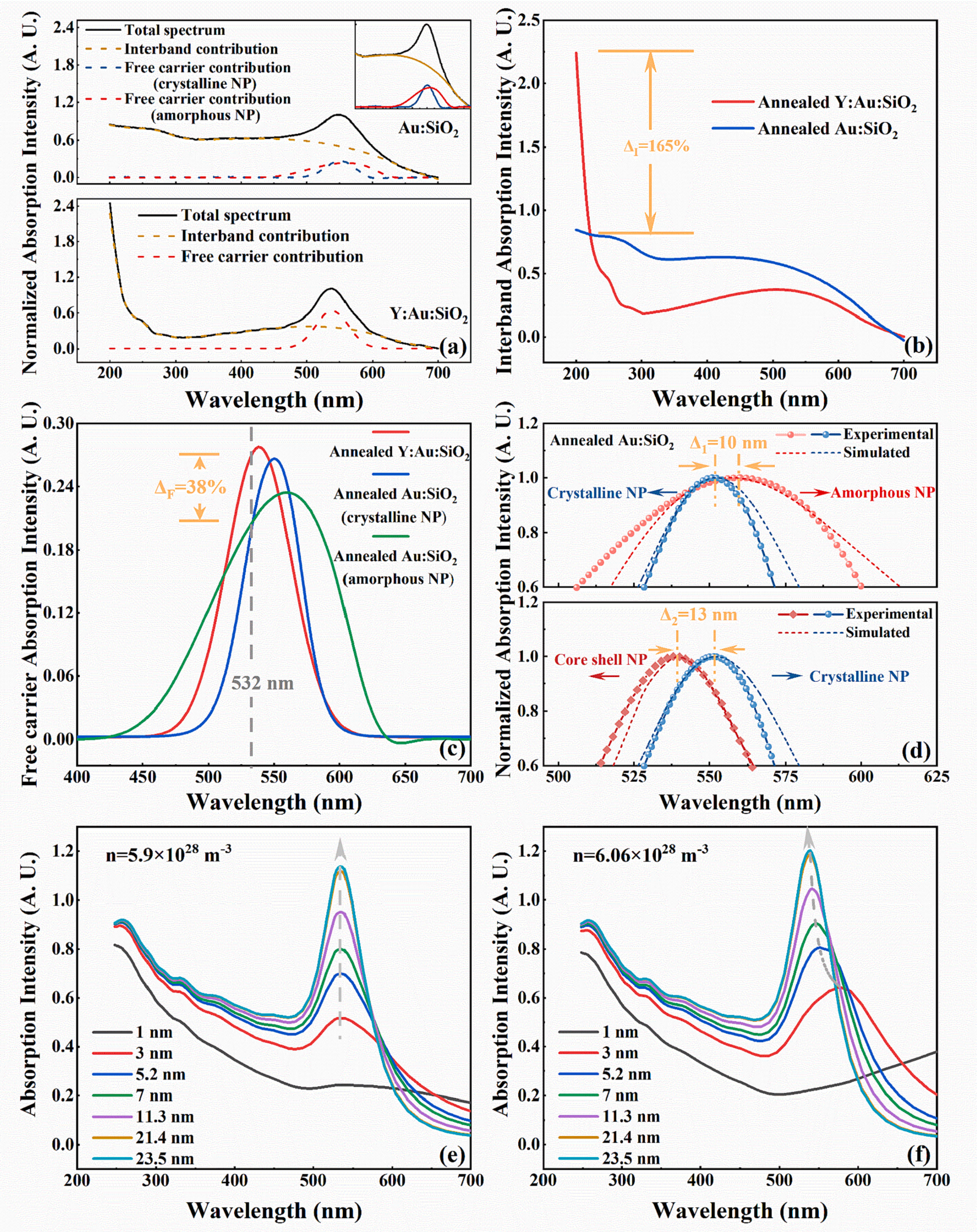

Fig. 4. (a) The LSPR absorption spectrum, (b) interband absorption spectrum and (c) free electron absorption spectrum of the sample annealed Au:SiO$_2$ and Y:Au:SiO$_2$. The LSPR absorption peaks are normalized and the insert is the enlarged image of the part of the spectrum. (d) The comparison of normalized free electron absorption peaks of crystalline Au NPs, amorphous Au NPs and core–shell NPs. The experimental and simulated results are displayed by point and dash line, respectively. The size-dependent absorption spectrum of (e) Au NP and (f) effective core–shell NP.

whole NP with modified free electron density and mobility due to the doping of Y atoms. Since the free electron density of Y and Au are calculated to be 6.06×10^{28} m^{-3} and 5.9×10^{28} m^{-3} (see the detailed calculation steps in Supplementary Material), electron transfer may occur between Au and Y atoms in the core–shell NPs, which will result in an enhanced free electron density at a balanced state. Based on the free electron density, the plasma frequency is calculated to be 1.39×10^{16} s^{-1}, larger than the value of Au (1.37×10^{16} s^{-1}). Thus, the LSPR effect should work at a shorter wavelength in theory, which has been proved on semiconductor plasmonic materials [46]. In addition, the resistivity of AuY bulk is calculated to be 540.22 nΩ·m, 24.4 times larger compared with that of Au bulk. With the modified free electron density and mobility, the LSPR absorption shows obvious size dependence. As seen in Fig. 4(f), the blue shift of the plasmonic peak is observed as the increase in NP size. Although the absorption peak often shows red shift as the metal NP size increases, it is not common for all the cases [47]. This red shift occurs only when the quantum size effect is dominant when the NP sizes are very small (a few nm or less). However, the mean diameter of effective core–shell NPs is 21.4 nm which means the quantum size effect is negligible. Instead, the size dependence of the absorption spectra is determined by the broadening and shift of the size-dependent complex dielectric function and the resonance conditions. The complex dielectric function strongly changes with the metal parameters. Both the blue and red shifts are induced depending on the metal parameters. Therefore, the physical mechanism of fine-tuning of plasmonics is believed to be the surface modification by the enhanced free electron density and mobility of Au@AuY/Au core–shell NPs. Noted that the existence of dispersed Y atoms in SiO_2 substrate may also contribute to the LSPR shift due to the fact that the refractive index of Y (1.2 [48]) is smaller than that of SiO_2 (1.46 [49]). However, it is not considered due to the very low concentration according to the element mapping image.

The spatial tailoring of plasmonics is verified by simulation of near-field distribution using discrete dipole approximation. As shown in Fig. 5(a) and (b), the near field intensity of core–shell NP (crystalline Au NP) is enhanced by 7.26 (6.34) times at 532 nm within (outside) the shell, and the near field intensity at the core area is greatly decreased which avoids the melting effect due to the photothermal effect. It means the spatial manipulation of plasmonics can be realized by designing the size of the shell for enhancement of optical properties. As seen in Fig. 5 (c), the core–shell NP array makes the near-field intensity present regular and continuous variation in space. In addition, the size dependence and diameter ratio dependence are investigated, respectively. Fig. 5(d) displays the near-field distribution for core–shell NP with various sizes, and the maximum enhancement factor indicates that smaller NP owns higher near-field intensity.

For NPs with different diameter ratios, it is shown that the maximum enhancement factor is enhanced as the diameter ratio increases, and the enhanced near field is always located in the shell of NPs. For the NP with a diameter ratio of 6:7, the maximum enhancement factor is as large as 37.4. Therefore, it indicates potential for further spatial modulation of plasmonics by size and diameter ratio.

To examine the application of fine plasmonic tuning of core–shell NPs in performance improvement of nonlinearity devices, the third-order nonlinear optical responses are measured by Z-scan measurement with an excitation wavelength of 532 nm. The experimental configuration is depicted in Fig. 6(a). With the movement of the sample along the laser propagation path between two lenses, the transmission varies with the z position of the sample (i.e., laser intensity). The saturation intensity and modulation depth are calculated according to the equation [50]:

$$\frac{dI}{dz} = \frac{-\alpha_0 I}{1 + I/I_{sat}} \tag{5}$$

where α_0 and I_{sat} are the linear absorption coefficient and saturation intensity.

Considering the different Au concentrations in different samples, the nonlinear results are analyzed by normalizing the Au volume content (see Supplementary Material). As shown in Fig. 6 (b) and (c), sample annealed Au:SiO_2 shows a maximum modulation depth of 7 % with a saturation intensity of 0.12 GW/cm^2, however, the modulation depth and saturation intensity of Au@AuY/Au core–shell NPs are increased by 57 % (from 7 % to 11 %) and 190 % (from 0.12 GW/cm^2 to 0.35 GW/cm^2), respectively. It is known that the third-order nonlinearity is closely related to the plasmonic absorption peak position and excitation laser wavelength, and the improved uniformity of NP size can also be another reason for the enhancement of third-order nonlinearity. More comparisons of Z-scan results between traditional Au NPs and NPs in this work are displayed in Table 1. As far as we can find, the size of Au NPs is usually much smaller in literature (such as No.3 and No.5 in Table 1), which results in a great decrease of modulation depth even in the case of No.5 with much higher concentration. Few works reported the characterization and fabrication of large Au NPs, e.g. Ichiro [53] etc., synthesized Au NPs with a similar mean diameter and size distribution with NPs in this work. Worth mentioning, the modulation of Au@AuY/Au core–shell NPs is enhanced by more than 4.4 times although the NP diameter is a little smaller than that in Reference [53]. The enhancement

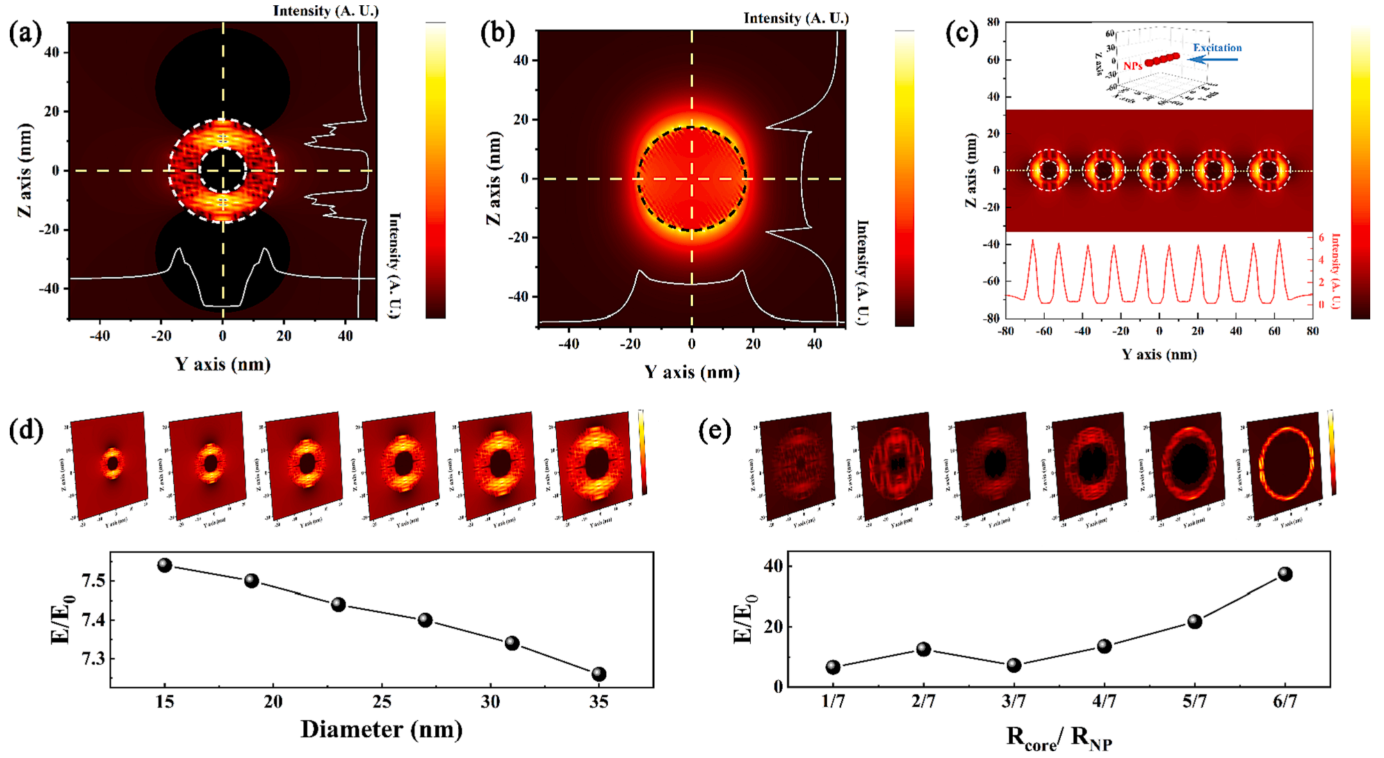

Fig. 5. The simulated near field distribution of (a) core–shell NP, (b) crystalline Au NP and (c) core–shell NP monolayer. The intensities of the field-enhancement factor along the dashed yellow line are shown as insert. (d) The size-dependent near field distribution of core–shell NP with diameter ratio R_{core}/R_{NP} of 3:7. (e) The diameter ratio is dependent on the field distribution of core–shell NP with a size of 35 nm. (For interpretation of the references to colour in this figure legend, the reader is referred to the web version of this article.)

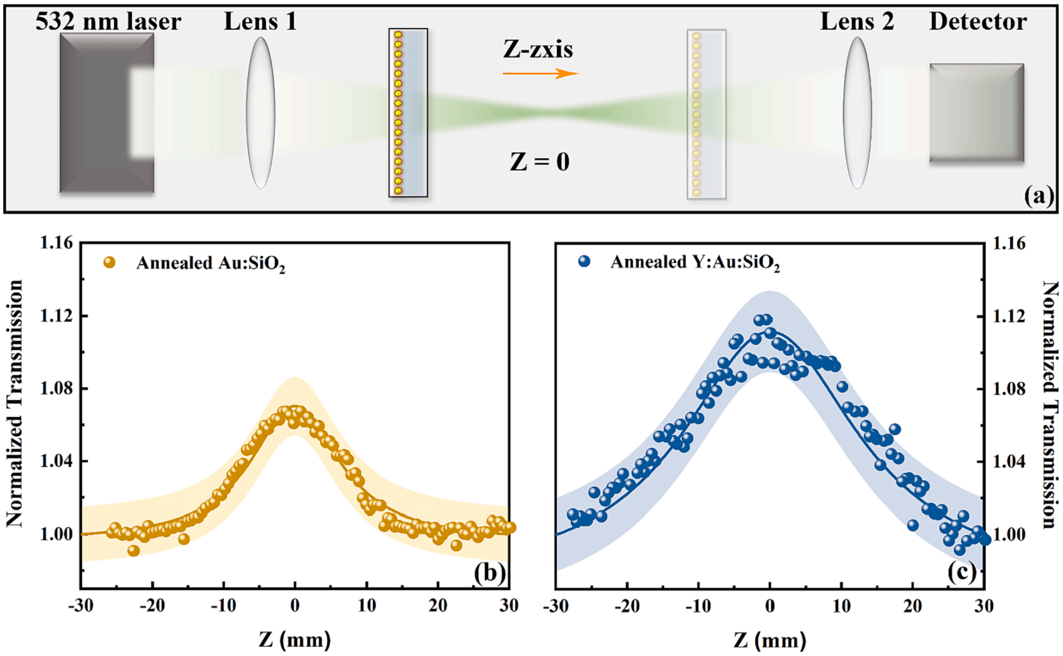

Fig. 6. (a) The experimental configuration of the Z-scan measurement system. The nonlinear optical response of samples (b) annealed Au:SiO$_2$ and (c) annealed Y:Au:SiO$_2$. The spectrum is analyzed by normalizing Au atomic content.

Table 1
The comparison of third-order nonlinearity of various Au NPs in literature and this work.

No.	NP	Bulk	Diameter	Au volume per cm^2	Modulation depth	Ref.
1	YAu	SiO$_2$	9.3 nm	0.52×10^{-6} cm^3	11 %	This work
2	Au	SiO$_2$	16.7 nm	1.37×10^{-6} cm^3	7(30)%	This work
3	Au	SiO$_2$	3.2 nm	0.95×10^{-6} cm^3	0.5(1.5)%	[51,52]
4	Au	SiO$_2$	12.9 nm	1.2×10^{-6} cm^3	2.5(10)%	[53]
5	Au	SiO$_2$	2 nm	2×10^{-6} cm^3	1.2(7)%	[54]

Note: The modulation depth is analyzed by normalizing Au content and the unprocessed data are displayed in brackets.

of nonlinear absorption indicates the significant potential of fine-tuning of plasmonics by Au@AuY/Au core–shell NPs.

4. Conclusions

In this work, the embedded Au@AuY/Au core–shell NPs are prepared in the silica matrix by sequential ion implantation with separate concentration distribution combined with thermal annealing, and the linear and nonlinear optical properties and corresponding tailoring mechanism of Au@AuY/Au core–shell NPs are further discussed. The small Au NPs formed by Au ion implantation and the implanted Y ions aggregate and migrate at high temperature, respectively. When the Y atom migrates to the Au NP region, it will combine with Au to form an AuY alloy wrapped around the Au core, after which it will fabricated to produce core–shell nanoparticles. The results of TEM characterization and DFT calculations show that the existence of the AuY/Au shell structure effectively delays the growth of the Au core and inhibits the formation of Au islands. Au@AuY/Au core–shell NPs show an obvious blue shift from 551 nm to 538 nm, which is attributed to the surface modification by the enhanced free electron density and mobility of Au@AuY/Au core–shell NPs. Meanwhile, the modulation depth and saturation intensity of Au@AuY/Au core–shell NPs are increased by 57 % and 190 %, respectively. The spatial manipulation of plasmonics is simulated by near-field simulation, which shows the unique enhanced near-field distribution in the shell. The size dependence and diameter ratio dependence are investigated as well, indicating the potential for further enhancement and flexible tailoring of plasmonics. The enhancement of nonlinear absorption indicates the significant potential of fine-tuning plasmonics by Au@AuY/Au core–shell NPs. This work provides a novel method for preparing core–shell nanoparticles with fine-tuning plasmonics, and enhancing the ability to tailor the optical properties of electrolytes, which is essential to design promising photonic devices with enhanced optical properties.

CRediT authorship contribution statement

Yong Liu: Investigation, Data curation, Formal analysis, Funding acquisition, Resources, Writing – original draft, Writing – review & editing. **Chi Pang:** Writing – review & editing. **Hiroshi Amekura:** Writing – review & editing. **Thomas Schumann:** Methodology, Writing – review & editing. **Peng Liu:** Investigation, Data curation, Formal analysis. **Zhixian Wei:** Data curation, Formal analysis. **Haocheng Liu:** Data curation, Formal analysis. **Rang Li:** Methodology, Conceptualization, Investigation, Methodology, Data curation, Formal analysis, Writing – original draft, Writing – review & editing.

Declaration of Competing Interest

The authors declare that they have no known competing financial interests or personal relationships that could have appeared to influence the work reported in this paper.

Data availability

Data will be made available on request.

Acknowledgements

This work was supported by the National Natural Science Foundation of China (grant number 12105159); Natural Science Foundation of

Shandong Province of China (grant number ZR2021QA102); China Postdoctoral Science Foundation funded project (grant number 2021M691915); the Alexander von Humboldt Foundation; the IBC center in HZDR institute. H.A. was supported by JSPS-KAKENHI (grant number 22K04990).

Appendix A. Supplementary data

Supplementary data to this article can be found online at https://doi.org/10.1016/j.apsusc.2023.157582.

References

[1] Y. Zhang, C. Min, X. Dou, X. Wang, H.P. Urbach, M.G. Somekh, X. Yuan, Plasmonic tweezers: for nanoscale optical trapping and beyond, Light Sci. Appl 10 (2021) 59, https://doi.org/10.1038/s41377-021-00474-0.

[2] M.L. Juan, M. Righini, R. Quidant, Plasmon nano-optical tweezers, Nat. Photonics 5 (2011) 349–356, https://doi.org/10.1038/nphoton.2011.56.

[3] K. Yao, X. Xin, C. Chueh, K. Chen, Y. Xu, A.K. Jen, Enhanced light-harvesting by integrating synergetic microcavity and plasmonic effects for high-performance ITO-free flexible polymer solar cells, Adv. Funct. Mater. 25 (2015) 567–574, https://doi.org/10.1002/adfm.201403297.

[4] M. Ali, F. Zhou, K. Chen, C. Kotzur, C. Xiao, L. Bourgeois, X. Zhang, D. R. MacFarlane, Nanostructured photoelectrochemical solar cell for nitrogen reduction using plasmon-enhanced black silicon, Nat. Commun. 7 (2016) 11335, https://doi.org/10.1038/ncomms11335.

[5] H. Wu, Y. Gao, P. Xu, X. Guo, P. Wang, D. Dai, L. Tong, Plasmonic nanolasers: Pursuing extreme lasing conditions on nanoscale, Adv. Opt. Mater. 7 (2019) 1900334, https://doi.org/10.1002/adom.201900334.

[6] T.P. Sidiropoulos, R. Röder, S. Geburt, O. Hess, S.A. Maier, C. Ronning, R.F. Oulton, Ultrafast plasmonic nanowire lasers near the surface plasmon frequency, Nat. Phys. 10 (2014) 870–876, https://doi.org/10.1038/nphys3103.

[7] Y. Liu, Z. Zhang, Y. Park, S.E. Lee, Ultraprecision imaging and manipulation of plasmonic nanostructures by integrated nanoscopic correction, Small 17 (2021) 2007610, https://doi.org/10.1002/smll.202007610.

[8] Y.U. Lee, S. Li, G.B.M. Wisna, J. Zhao, Y. Zeng, A.R. Tao, Z. Liu, Hyperbolic material enhanced scattering nanoscopy for label-free super-resolution imaging, Nat. Commun. 13 (2022) 6631, https://doi.org/10.1038/s41467-022-34553-6.

[9] L. Wang, M. Hasanzadeh Kafshgari, M. Meunier, Optical properties and applications of plasmonic-metal nanoparticles, Adv. Funct. Mater. 30 (2020) 2005400, https://doi.org/10.1002/adfm.202005400.

[10] P. Rohani, S. Banerjee, S. Sharifi Asl, M. Malekzadeh, R. Shahbazian Yassar, S. J. Billinge, M.T. Swihart, Synthesis and properties of plasmonic boron-hyperdoped silicon nanoparticles, Adv. Funct. Mater. 29 (2019) 1807788.

[11] M. Proença, J. Borges, M.S. Rodrigues, D.I. Meira, P. Sampaio, J.P. Dias, P. Pedrosa, N. Martin, N. Bundaleski, O.M. Teodoro, Nanocomposite thin films based on Au-Ag nanoparticles embedded in a CuO matrix for localized surface plasmon resonance sensing, Appl. Surf. Sci. 484 (2019) 152–168, https://doi.org/10.1016/j.apsusc.2019.04.085.

[12] J. Chen, Y. Ren, T. Hu, T. Xu, Q. Xu, Fabrication and application of substoichiometric tungsten oxide with tunable localized surface plasmon resonances, Appl. Surf. Sci. 465 (2019) 517–525, https://doi.org/10.1016/j.apsusc.2018.09.140.

[13] J.M. Poumirol, C. Majorel, N. Chery, C. Girard, P.R. Wiecha, N. Mallet, R. Monflier, G. Larrieu, F. Cristiano, A.S. Royet, Hyper-doped silicon nanoantennas and metasurfaces for tunable infrared plasmonics, ACS Photonics 8 (2021) 1393–1399, https://doi.org/10.1021/acsphotonics.1c00019.

[14] B. Tandon, S.L. Gibbs, C. Dean, D.J. Milliron, Highly Responsive Plasmon Modulation in Dopant-Segregated Nanocrystals, Nano Lett. (2022), https://doi.org/10.1021/acs.nanolett.2c04199.

[15] Z. Li, J. Nan, X. Zhang, S. Ye, H. Shen, S. Wang, L. Fang, P. Xue, J. Zhang, B. Yang, Modulate the morphology and spectroscopic property of gold nanoparticle arrays by polymer-assisted thermal treatment, J. Phys. Chem. C 119 (2015) 11839–11845, https://doi.org/10.1021/acs.jpcc.5b02263.

[16] P. Pandey, S. Kunwar, M. Sui, S. Bastola, J. Lee, Modulation of morphology and optical property of multi-metallic PdAuAg and PdAg alloy nanostructures, Nanoscale Res. Lett. 13 (2018) 1–12, https://doi.org/10.1186/s11671-018-2551-0.

[17] C. Pang, R. Li, N. Dong, Z. Li, J. Wang, F. Ren, F. Chen, Plasmonic core-shell nano-heterostructures with temperature-dependent optical nonlinearity, Nanoscale 12 (2020) 22995–23002, https://doi.org/10.1039/D0NR05176D.

[18] R. Li, C. Pang, Z. Li, F. Chen, Plasmonic nanoparticles in dielectrics synthesized by ion beams: optical properties and photonic applications, Adv. Opt. Mater. 8 (2020) 1902087, https://doi.org/10.1002/adom.201902087.

[19] C. Pang, R. Li, Z. Li, N. Dong, F. Ren, J. Wang, F. Chen, A novel hierarchical nanostructure for enhanced optical nonlinearity based on scattering mechanism, Small 16 (2020) 2003172, https://doi.org/10.1002/smll.202003172.

[20] C.F. Hoener, K.A. Allan, A.J. Bard, A. Campion, M.A. Fox, T.E. Mallouk, S. E. Webber, J.M. White, Demonstration of a shell-core structure in layered cadmium selenide-zinc selenide small particles by x-ray photoelectron and Auger spectroscopies, J. Phys. Chem. C 96 (1992) 3812–3817, https://doi.org/10.1021/j100188a045.

[21] I. Honma, T. Sano, H. Komiyama, Surface-enhanced Raman scattering (SERS) for semiconductor microcrystallites observed in silver-cadmium sulfide hybrid particles, J. Phys. Chem. C 97 (1993) 6692–6695, https://doi.org/10.1021/j100127a020.

[22] R. Ghosh Chaudhuri, S. Paria, Core/shell nanoparticles: classes, properties, synthesis mechanisms, characterization, and applications, Chem. Rev. 112 (2012) 2373–2433, https://doi.org/10.1021/cr100449n.

[23] M.B. Gawande, A. Goswami, T. Asefa, H. Guo, A.V. Biradar, D. Peng, R. Zboril, R. S. Varma, Core-shell nanoparticles: synthesis and applications in catalysis and electrocatalysis, Chem. Soc. Rev. 44 (2015) 7540–7590, https://doi.org/10.1039/C5CS00343A.

[24] G. Jia, R. Xu, X. Mu, C. Liu, Zn ion post-implantation-driven synthesis of CuZn alloy nanoparticles in Cu-preimplanted silica and their thermal evolution, ACS Appl. Mater. Interfaces 5 (2013) 13055–13062, https://doi.org/10.1021/am403941n.

[25] R. Das, R. Soni, Highly stable In@ SiO_2 core-shell nanostructures for ultraviolet surface-enhanced Raman spectroscopy, Appl. Surf. Sci. 489 (2019) 755–765, https://doi.org/10.1016/j.apsusc.2019.06.003.

[26] H. Chen, Y. Wang, X. Zhang, S. Song, K. Zhang, Z. Xiong, L. Ji, H. Dai, D. Wang, J. Lu, Structure analysis of bimetallic Co-Au nanoparticles formed by sequential ion implantation, Appl. Surf. Sci. 378 (2016) 191–195, https://doi.org/10.1016/j.apsusc.2016.03.233.

[27] J.W. Liaw, G. Liu, Y. Ku, M. Kuo, Plasmon-enhanced photothermal and optomechanical deformations of a gold nanoparticle, Nanomaterials 10 (2020) 1881, https://doi.org/10.3390/nano10091881.

[28] Y. Huang, X. Xie, M. Li, M. Xu, J. Long, Copper circuits fabricated on flexible polymer substrates by a high repetition rate femtosecond laser-induced selective local reduction of copper oxide nanoparticles, Opt. Express 29 (2021) 4453–4463, https://doi.org/10.1364/OE.416772.

[29] F. Chen, H. Amekura, Y. Jia, Ion irradiation of dielectrics for photonic applications, Springer (2020), https://doi.org/10.1007/978-981-15-4607-5.

[30] F. Ren, X.H. Xiao, G.X. Cai, J.B. Wang, C.Z. Jiang, Engineering embedded metal nanoparticles with ion beam technology, Appl. Phys. A 96 (2009) 317–325, https://doi.org/10.1007/s00339-009-5205-3.

[31] Y. Liu, X. Han, J. Zhao, J. Sun, Q. Huang, X. Wang, P. Liu, Structure Formation and Regulation of Au Nanoparticles in $LiTaO_3$ by Ion Beam and Thermal Annealing Techniques, Nanomaterials 12 (2022) 4028, https://doi.org/10.3390/nano12224028.

[32] W. Wesch, E. Wendler, Ion beam modification of solids, Series in Surf. Sci. 61 (2016), https://doi.org/10.1007/978-3-319-33561-2.

[33] Y. Zhang, J. Lian, Z. Zhu, W.D. Bennett, L.V. Saraf, J.L. Rausch, C.A. Hendricks, R. Ewing, W.J. Weber, Response of strontium titanate to ion and electron irradiation, J. Nucl. Mater. 389 (2009) 303–310, https://doi.org/10.1016/j.jnucmat.2009.02.014.

[34] J.F. Ziegler, M.D. Ziegler, J.P. Biersack, SRIM-The stopping and range of ions in matter, Nucl. Instrum. Methods Phys. Res. Sect. B 268 (2010) (2010) 1818–1823, https://doi.org/10.1016/j.nimb.2010.02.091.

[35] S. Grimme, J. Antony, S. Ehrlich, H. Krieg, A consistent and accurate ab initio parametrization of density functional dispersion correction (DFT-D) for the 94 elements H-Pu, J. Chem. Phys. 132 (2010), 154104, https://doi.org/10.1063/1.3382344.

[36] S. Grimme, S. Ehrlich, L. Goerigk, Effect of the damping function in dispersion corrected density functional theory, J. Comput. Chem. 32 (2011) 1456–1465, https://doi.org/10.1002/jcc.21759.

[37] B.T. Draine, P.J. Flatau, Discrete-dipole approximation for scattering calculations, J. Opt. Soc. Am. A 11 (1994) 1491–1499, https://doi.org/10.1364/JOSAA.11.001491.

[38] P.W. Voorhees, The theory of Ostwald ripening, J. Stat. Phys. 38 (1985) 231–252, https://doi.org/10.1007/BF01017860.

[39] Y. Liu, J. Sun, X. Han, Q. Huang, E. Zarkadoula, M.L. Crespillo, N. Gao, X. Wang, P. Liu, Microstructure and hardness evolution induced by annealing of ion irradiated LiTaO3, Appl. Surf. Sci. 614 (2023), 156222, https://doi.org/10.1016/j.apsusc.2022.156222.

[40] F. Ren, C. Jiang, C. Liu, J. Wang, T. Oku, Controlling the morphology of Ag nanoclusters by ion implantation to different doses and subsequent annealing, Phys. Rev. Lett. 97 (2006), 165501, https://doi.org/10.1103/PhysRevLett.97.165501.

[41] L. Minervini, M.O. Zacate, R.W. Grimes, Defect cluster formation in M_2O_3-doped CeO_2, Solid State Ion. 116 (1999) 339–349, https://doi.org/10.1016/S0167-2738(98)00359-2.

[42] B. Balamurugan, T. Maruyama, Evidence of an enhanced interband absorption in Au nanoparticles: size-dependent electronic structure and optical properties, Appl. Phys. Lett. 87 (2005), 143105, https://doi.org/10.1063/1.2077834.

[43] G. Mie, Beiträge zur Optik trüber Medien, speziell kolloidaler Metallösungen, Annalen der Physik 330 (1908) 377–445, https://doi.org/10.1002/andp.19083300302.

[44] H. Amekura, B. Johannessen, D. Sprouster, M. Ridgway, Amorphization of Cu nanoparticles: Effects on surface plasmon resonance, Appl. Phys. Lett. 99 (2011), 043102, https://doi.org/10.1063/1.3615307.

[45] K.L. Kelly, E. Coronado, L.L. Zhao, G.C. Schatz, The optical properties of metal nanoparticles: the influence of size, shape, and dielectric environment, J. Chem. Phys. B 107 (2003) 668–677, https://doi.org/10.1021/jp026731y.

[46] A. Boltasseva, H.A. Atwater, Low-loss plasmonic metamaterials, Science 331 (2011) 290–291, https://doi.org/10.1126/science.1198258.

[47] H. Amekura, Y. Takeda, N. Kishimoto, Criteria for surface plasmon resonance energy of metal nanoparticles in silica glass, Nucl. Instrum. Methods Phys. Res. B 222 (2004) 96–104, https://doi.org/10.1016/j.nimb.2004.01.003.

[48] B. Sae-Lao, R. Soufli, Measurements of the refractive index of yttrium in the 50–1300-eV energy region, Appl. Opt. 41 (2002) 7309–7316, https://doi.org/10.1364/AO.41.007309.

[49] J. Swart, J. Diniz, I. Doi, M. de Moraes, Modification of the refractive index and the dielectric constant of silicon dioxide by means of ion implantation, Nucl. Instrum. Methods. Phys. Res. B 166 (2000) 171–176, https://doi.org/10.1016/S0168-583X(99)00650-3.

[50] M. Sheik-Bahae, A.A. Said, T.H. Wei, D.J. Hagan, E.W. Van Stryland, Sensitive measurement of optical nonlinearities using a single beam, IEEE J. Sel. Top. Quantum Electron. 26 (1990) 760–769, https://doi.org/10.1109/3.53394.

[51] A. Ryasnyanskiy, B. Palpant, S. Debrus, U. Pal, A. Stepanov, Nonlinear optical properties of gold nanoparticles dispersed in different optically transparent matrices, Phys. Solid State 51 (2009), https://doi.org/10.1134/S1063783409010065.

[52] N. Pinçon, B. Palpant, D. Prot, E. Charron, S. Debrus, Third-order nonlinear optical response of Au: SiO_2 thin films: Influence of gold nanoparticle concentration and morphologic parameters, Eur. Phys. J. D 19 (2002) 395–402, https://doi.org/10.1140/epjd/e20020085.

[53] I. Tanahashi, H. Inouye, A. Mito, Femtosecond nonlinear optical properties of Au/SiO_2 composite thin films prepared by a sputtering method, Jpn. J. Appl. Phys. 42 (2003) 3467, https://doi.org/10.1143/JJAP.42.3467.

[54] S. Debrus, J. Lafait, M. May, N. Pinçon, D. Prot, C. Sella, J. Venturini, Z-scan determination of the third-order optical nonlinearity of gold: silica nanocomposites, J. Appl. Phys. 88 (2000) 4469–4475, https://doi.org/10.1063/1.1290260.